WILEY | Hindawi

*Research Article*

# Facile Synthesis of Indium Sulfide/Flexible Electrospun Carbon Nanofiber for Enhanced Photocatalytic Efficiency and Its Application

**Liu Han,[1,2] Haohao Dong,[1] Dong Mao,[1,2] Baolv Hua,[1] Qinyu Li,[1] and Dong Fang[1,2]**

[1]*School of Chemistry and Environmental Engineering, Yancheng Teachers University, Yancheng 224002, China*
[2]*College of Chemical Engineering, Nanjing Tech University, Nanjing 210009, China*

Correspondence should be addressed to Dong Fang; fangd@yctu.edu.cn

Heterojunction system has been proved as one of the best architectures for photocatalyst owing to extending specific surface area, expanding spectral response range, and increasing photoinduced charges generation, separation, and transmission, which can provide better light absorption range and higher reaction site. In this paper, Indium Sulfide/Flexible Electrospun Carbon Nanofiber ($In_2S_3$/CNF) heterogeneous systems were synthesized by a facile one-pot hydrothermal method. The results from characterizations of SEM, TEM, XRD, Raman, and UV-visible diffuse reflectance spectroscopy displayed that flower-like $In_2S_3$ was deposited on the hair-like CNF template, forming a one-dimensional nanofibrous network heterojunction photocatalyst. And the newly prepared $In_2S_3$/CNF photocatalysts exhibit greatly enhanced photocatalytic activity compared to pure $In_2S_3$. In addition, the formation mechanism of the one-dimensional heterojunction $In_2S_3$/CNF photocatalyst is discussed and a promising approach to degrade Rhodamine B (RB) in the photocatalytic process is processed.

## 1. Introduction

Nowadays, it is a huge challenge for people to deal with the organic pollutant in the energy crisis environment [1–3]. Certainly, photocatalytic as a novel solution has aroused great interest for people. It has been considered as one of the most effective ways for the solar energy conversion and the destruction of organic pollutant [4, 5]. Up to now, numerous experiments of the degradation of organic pollutants by using photocatalysts have been researched. However, the photocatalytic activity of pure photocatalyst is limited by its low efficiency of light absorption, difficult migration, and high recombination probability of photogenerated electron-hole pairs, and the development of photocatalytic technology is still limited for the photocatalyst [6–8]. Therefore, it is urgent and indispensable to find a novel photocatalyst to improve both the photochemical activity and the stability.

$In_2S_3$, as a typical III–VI group sulfide, is an n-type semiconductor with a band gap of 2.0–2.3 eV corresponding to visible light region which attracted intense interest for

optical, photoconductive, and optoelectronic applications. Furthermore, $In_2S_3$ shows property of high photosensitivity and photoconductivity, stable chemical and physical characteristics, and low toxicity; it has great potential for visible-light-driven photodegradation of pollutants [9, 10]. Realistically, the narrow band gap and the rapid recombination of photogenerated electron-hole pairs causing poor quantum yield are similar to other visible light photocatalysts [11–14]. To meet the practical application requirements, it is urgent and important to enhance the photocatalytic efficiency of $In_2S_3$. Up to now, many attempts have been explored to improve the photocatalytic performance of $In_2S_3$, such as metal ions doping, coupling with other semiconductors, and carbon materials-based assemblies [15, 16].

As a viable alternative route to boost the efficiency of photocatalysts, CNF-based assemblies have aroused attention [17–19]. CNF is easily synthesized by electrospinning with a large theoretical specific surface area and high intrinsic electron mobility; it possesses physicochemical, superior electronic, mechanical character, and high absorption properties.
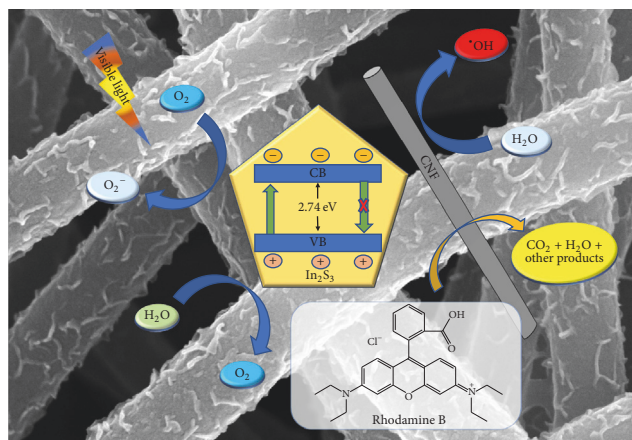
Scheme 1: Postulated mechanism of the visible-light-induced photodegradation of RB with $In_2S_3$/CNF.

In particular, compared with traditional carbon nanofibers obtained by other physical and chemical methods, the carbon nanofibers synthesized by electrospinning (CNF) have stronger electronic transport properties [20, 21]. Therefore, it is an ideal method to enhance photocatalytic activity by coupling $In_2S_3$ with CNF to construct $In_2S_3$/CNF.

In this work, the CNF was fabricated by electrospinning technique, and $In_2S_3$/CNF composites were fabricated through a one-pot hydrothermal reaction as shown in Scheme 1. The photogenerated electrons on the conduction bands (CB) of $In_2S_3$ could easily be transferred to CNF for the positive synergetic effect, in brief, because the formation of interface junction can improve the optical absorption property and simultaneously facilitate the separation of photoinduced electron-hole pairs. In addition, the promising applications of $In_2S_3$/CNF composites have excellent performance for the degradation of organic pollutants. This study shows a reliable method to degrade organic pollutants.

## 2. Experimental Section

*2.1. Materials.* All the reagents were of analytical grade and were used as received without further purification. $InCl_3 \cdot 5H_2O$, thioacetamide (TAA), and other chemicals were of analytical grade and purchased from Sinopharm Chemical Reagents Co., Ltd. Polyacrylonitrile (PAN) ($M_w = 150,000 \, g \, mol^{-1}$) was purchased from Sigma-Aldrich.

*2.2. Fabrication of CNF.* According to previous reports [22], PAN nanofiber was synthesized from PAN by a modified electrospinning method. Firstly, 1 g PAN was dissolved completely in 9 mL *N,N*-dimethylformamide (DMF). Then, the mixture was transferred to 5 mL plastic syringe by two times for electrospinning (voltage: 20 kV, injection rate: $0.2 \, mm \, min^{-1}$). In order to obtain CNF, the PAN was carbonized at 500°C for 2 h under an inert atmosphere with a heating rate of $2 \, K \, min^{-1}$.

*2.3. Fabrication of $In_2S_3$/CNF.* $In_2S_3$/CNF with different $In_2S_3$ loadings was then prepared by a facile one-pot hydrothermal method. Briefly, a certain amount of $InCl_3 \cdot 5H_2O$ (351, 702, or 1053 mg) and thioacetamide (120 mg) was dissolved in ethyl alcohol (40 mL) under ultrasound conditions. The CNF (50 mg) was then immersed in the above solution, which was then transferred to a Teflon-lined autoclave and heated in a homogeneous reactor at 180°C for 12 h. According to this method, different weight ratios of the $In_2S_3$ to g-CNF samples were synthesized and labeled as $In_2S_3$/CNF-1, $In_2S_3$/CNF-2, and $In_2S_3$/CNF-4, respectively. By controlled trial, the $In_2S_3$ was fabricated by the same method.

*2.4. Characterization.* Scanning electron microscopy (SEM; Hitachi S-4800) coupled with X-ray energy dispersive spectroscopy (SEM-EDS) and transmission electron microscopy (TEM; Hitachi H600) were used to observe the morphology, structure, and size of the $In_2S_3$/CNF and its components. The effect of the $In_2S_3$ and CNF contents of $In_2S_3$/CNF on its structural properties were investigated by X-ray photoelectron spectroscopy (XPS; Axis Ultra HAS), Raman (Raman; Axis Ultra HAS), and X-ray diffraction (XRD; X' Pert-Pro MPD). The optical properties and the dye concentration were determined by UV-visible diffuse reflectance spectroscopy (UV-vis DRS, Shimadzu UV-3600).

*2.5. Photocatalytic Activity Measurements.* The photocatalytic activities of samples were evaluated by measuring the photodegradation of Rhodamine B (RB) under visible light. In a typical measurement, 40 mg photocatalysts were suspended in 100 mL of 50 ppm aqueous solution of RB. The solution was stirred in the dark for 30 min to obtain a good dispersion and to reach the adsorption–desorption equilibrium between the organic molecules and the catalysts surface [23]. Then the suspension was illuminated with a 250 W xenon lamp. The concentration change of RB was monitored by measuring the UV-vis absorption of the suspensions at regular intervals (take samples every 10 minutes). The suspension was filtered to remove the photocatalysts before
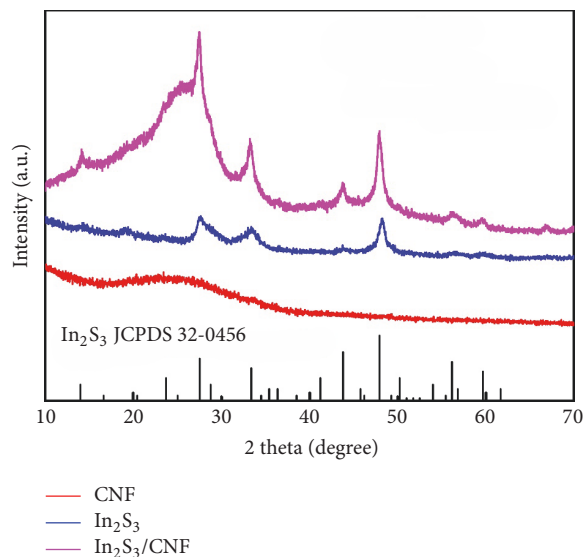
FIGURE 1: XRD patterns of $In_2S_3$, CNF, and $In_2S_3$/CNF-2.

measurement. The concentrations of RB in the reacting solutions were analyzed at $\lambda$ = 554 nm [24]. The photocatalytic activity was analyzed by the time profiles of $C/C_0$, where $C$ is the concentration of RB at the irradiation time $t$ and $C_0$ is the concentration in the absorption equilibrium of the photocatalysts before irradiation, respectively. The normalized temporal concentration changes ($C/C_0$) of RB are proportional to the normalized maximum absorbance ($A/A_0$), which can be derived from the change in the RB absorption profile at a given time interval [25].

## 3. Results and Discussion

The X-ray diffraction (XRD) patterns of pure CNF, $In_2S_3$, and $In_2S_3$ are shown in Figure 1. All of the diffraction peaks can be indexed to that of $In_2S_3$ with a cubic phase structure (JCPDS, number 32-0456). Peaks at $2\theta$ of 14, 27, 33, 44, 48, 56, and 60° in the XRD patterns of $In_2S_3$/CNF-2 and $In_2S_3$ correspond to the (111), (311), (400), (511), (533), and (444) planes of $In_2S_3$, respectively. The XRD patterns of the $In_2S_3$/CNF-2 heterostructures show all the diffraction peaks assigned to hexagonal $In_2S_3$ except the peak at 25° which corresponds to (130) plane of orthorhombic CNF, indicating the existence of $In_2S_3$ and CNF in the $In_2S_3$/CNF-2 heterostructures. Moreover, the intensities of the corresponding diffraction peaks of $In_2S_3$ strengthened gradually along with the addition of the CNF in the $In_2S_3$/CNF-2 composites; the formation of heterostructures can be demonstrated.

The morphology of the $In_2S_3$ and $In_2S_3$/CNF-2 was analyzed by SEM and TEM. The flower-like $In_2S_3$ with an average diameter of 5 um possesses porous structures due to the aggregation of a certain amount of nanosheets (Figure 2(a)). The TEM image of Figure 2(b) further confirms the result. The SEM image of electrospun CNF is shown in

Figure 2(c), which shows that the average diameter is about 300 nm and there is no defect in a smooth surface. As shown in TEM images (Figure 2(d)), it is clear that the surface of $In_2S_3$/CNF-2 is uniformly covered by the ultrathin $In_2S_3$ nanosheets after hydrothermal treatment. Further, there is no aggregation found in the surface of $In_2S_3$/CNF-2 composites.

The EDX spectrum shown in Figure 2(e) reveals the presence of In and S elements in a mass fraction ratio of 4.47% : 1.61%, which is close to the expected stoichiometry for $In_2S_3$ (Au signal is from FTO substrate).

Figure 3 shows that the different concentration of $In_2S_3$ deposited on the surface of CNF nanofibers. A small amount of nanoplate-like $In_2S_3$ was found on the smooth surface of CNF nanofibers, which correspond to low concentration. As the concentration increases (Figures 3(c) and 3(d)), $In_2S_3$ nanosheets with curled shapes grow vertically on the nanofiber surface and with a uniform distribution. In addition, the surface of nanofiber also turns from smooth to rough. As shown in Figures 3(e) and 3(f), serious aggregation occurred and thick layer $In_2S_3$ nanosheets were observed after further increasing the $In_2S_3$ concentration. The rapid nucleation of $In_2S_3$ at high concentration can be demonstrated.

XPS measurements were carried out to testify the chemical composition and chemical states of elements in $In_2S_3$/CNF-2 heterostructure photocatalyst [26]. The full-scale XPS spectrum for $In_2S_3$/CNF-2 sample is shown in Figure 4(a), in which the In, S, and C elements could be detected and no other impurities were observed. Figures 4(b), 4(c), and 4(d) show the high-resolution XPS spectra for $In_2S_3$/CNF sample. The XPS peaks (Figure 4(b)) at 444.1 and 452.7 eV correspond to the $In3d_{5/2}$ and $In3d_{3/2}$ states [27], respectively. The peak at 161.9 eV in Figure 4(c) corresponds to the $S2p_{3/2}$ state of $S_2^{2-}$ moieties. The peak at 284.8 eV in Figure 4(d) corresponds to the C1s state. The above XPS
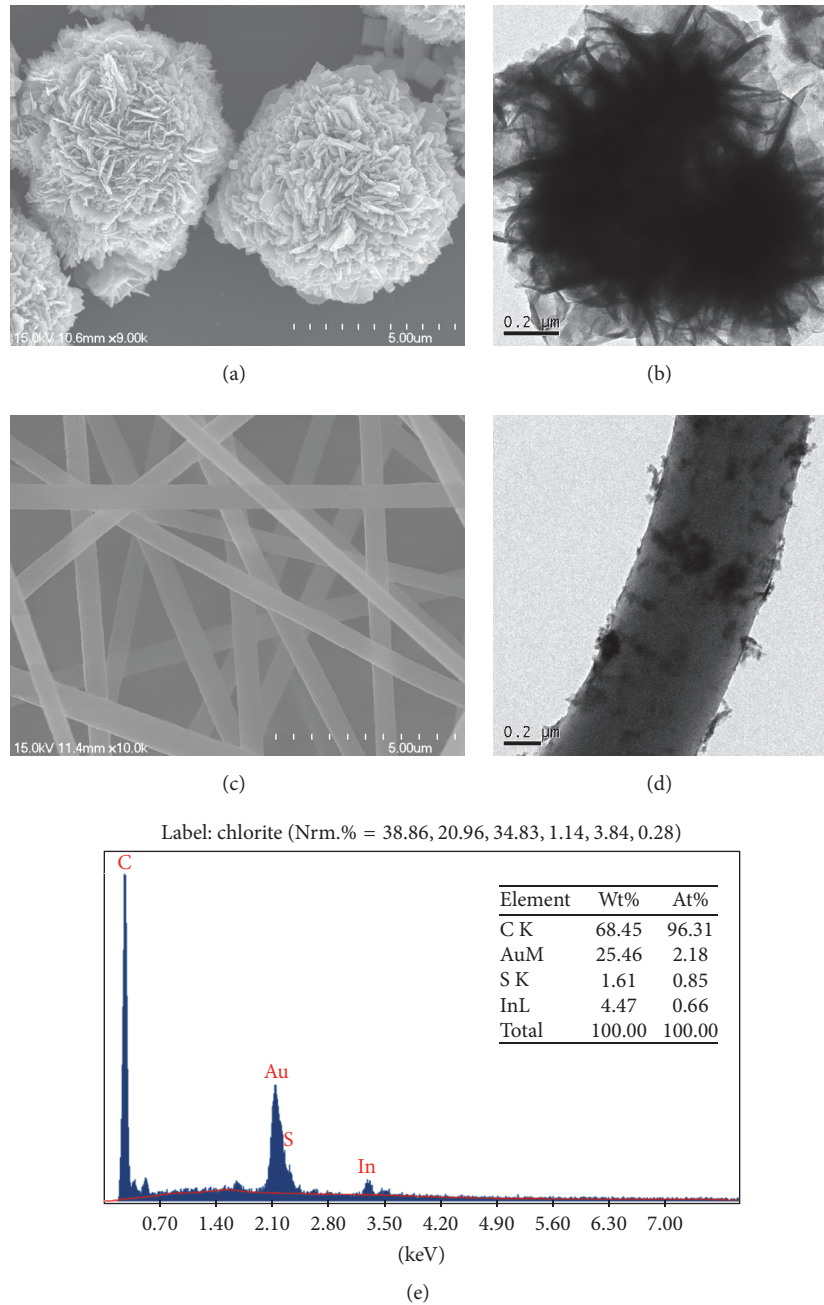
(a)

(b)

(c)

(d)

Label: chlorite (Nrm.% = 38.86, 20.96, 34.83, 1.14, 3.84, 0.28)

| Element | Wt% | At% |
|---------|--------|--------|
| C K | 68.45 | 96.31 |
| AuM | 25.46 | 2.18 |
| S K | 1.61 | 0.85 |
| InL | 4.47 | 0.66 |
| Total | 100.00 | 100.00 |

0.70  1.40  2.10  2.80  3.50  4.20  4.90  5.60  6.30  7.00

(keV)

(e)

FIGURE 2: SEM images of $In_2S_3$ and CNF ((a) and (c)), TEM images of $In_2S_3$ and $In_2S_3$/CNF-2 ((b) and (d)), and EDX pattern of $In_2S_3$/CNF-2 (e).

results confirm that the composites are composed of $In_2S_3$ and CNF.

Raman analysis was explored to confirm the presence of CNF and $In_2S_3$ in $In_2S_3$/CNF-2 sample (Figure 5). D-peak (D band) represents the defects of C atomic lattice, and G-peak (G band) represents the expansion vibration of the surface of C atom $sp^2$ hybridization. And the representative Raman spectrum in a range of Raman shift from 100 to 2000 $cm^{-1}$ of the CNF shows mainly two peaks centered around 1369 $cm^{-1}$ (D band) and 1590 $cm^{-1}$ (G band) for CNF. Furthermore, the degree of fibrosis can be measured by the intensity ratio of the G to D band ($I_G/I_D$) [28–30], where $I_G/I_D$ is the intensity ratio of D-peak and G-peak. A slight increase in the $I_G/I_D$ ratio is observed in the spectrum of $In_2S_3$/CNF-2 composites, the D/G integral intensity ratio ($I_D/I_G$) for CNF in the $In_2S_3$/CNF-2 sample (1.13) is slightly higher than that of CNF (1.12), it is indicated that a certain amount of $In_2S_3$ deposited on the surface of CNF during the chemical reduction process,
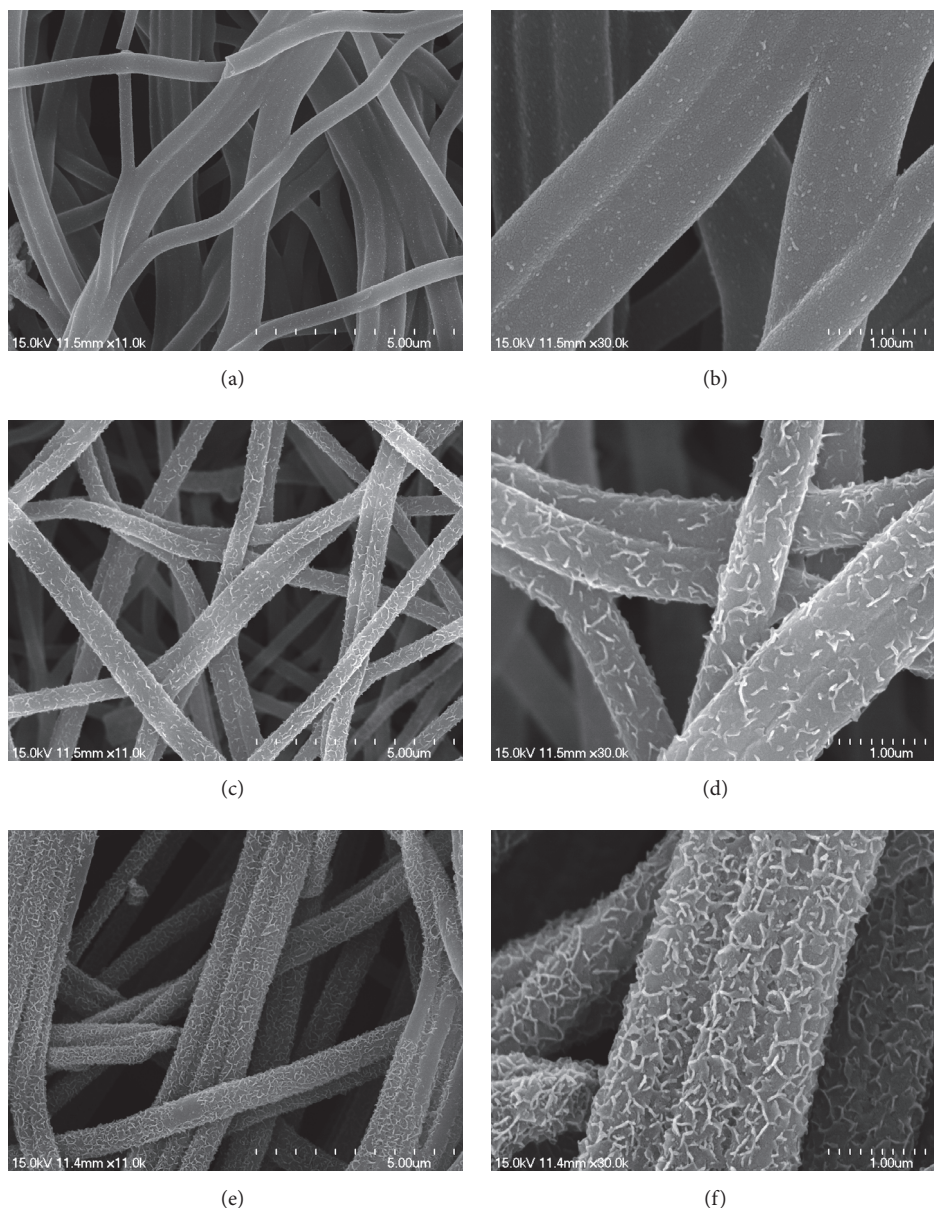
(a)

(b)

(c)

(d)

(e)

(f)

FIGURE 3: Low- (a, c, e) and high- (b, d, f) magnification SEM images of low concentration of $In_2S_3$ loaded on CNF ((a) and (b)), moderate concentration of $In_2S_3$ loaded on CNF ((c) and (d)), and high concentration of $In_2S_3$ loaded on CNF ((e) and (f)).

and the conjugated CNF network was reestablished [31]. The two peaks for D and G band of the composite no shift appears, indicating that only a small amount of $In_2S_3$ deposited on the surface of CNF.

The optical properties of the three samples were detected by UV-vis DRS absorption spectroscopy (Figure 6). Obviously, CNF shows the best performance and its absorption peaks appear in the visible light and UV light regions. It should be noted that $In_2S_3$/CNF-2 with the addition of CNF showed an increased photocatalytic performance compared to $In_2S_3$ (Figure 6(a)). The band gap energy ($E_g$) of samples was calculated by Tauc's equation

[32, 33] and the result was shown in Figure 6(b); the $E_g$ values of $In_2S_3$ and $In_2S_3$/CNF-2 in Figure 6(b) are approximately 2.70 and 3.08 eV. The band gap of $In_2S_3$/CNF-2 was higher than $In_2S_3$, which is close to the value of $In_2S_3$ and $In_2S_3$/CNF reported in other literatures [10, 34]. Thus, it is indicated that the as-prepared $In_2S_3$/CNF-2 heterojunction structures have the appropriate $E_g$ for photodegradation of organic pollutants under visible light irradiation.

In order to detect the ability of photodegradation, different photocatalysts were used to photodegrade organic pollutant under visible light irradiation, then the samples of products were analyzed. The results are shown in Figures 7(a)
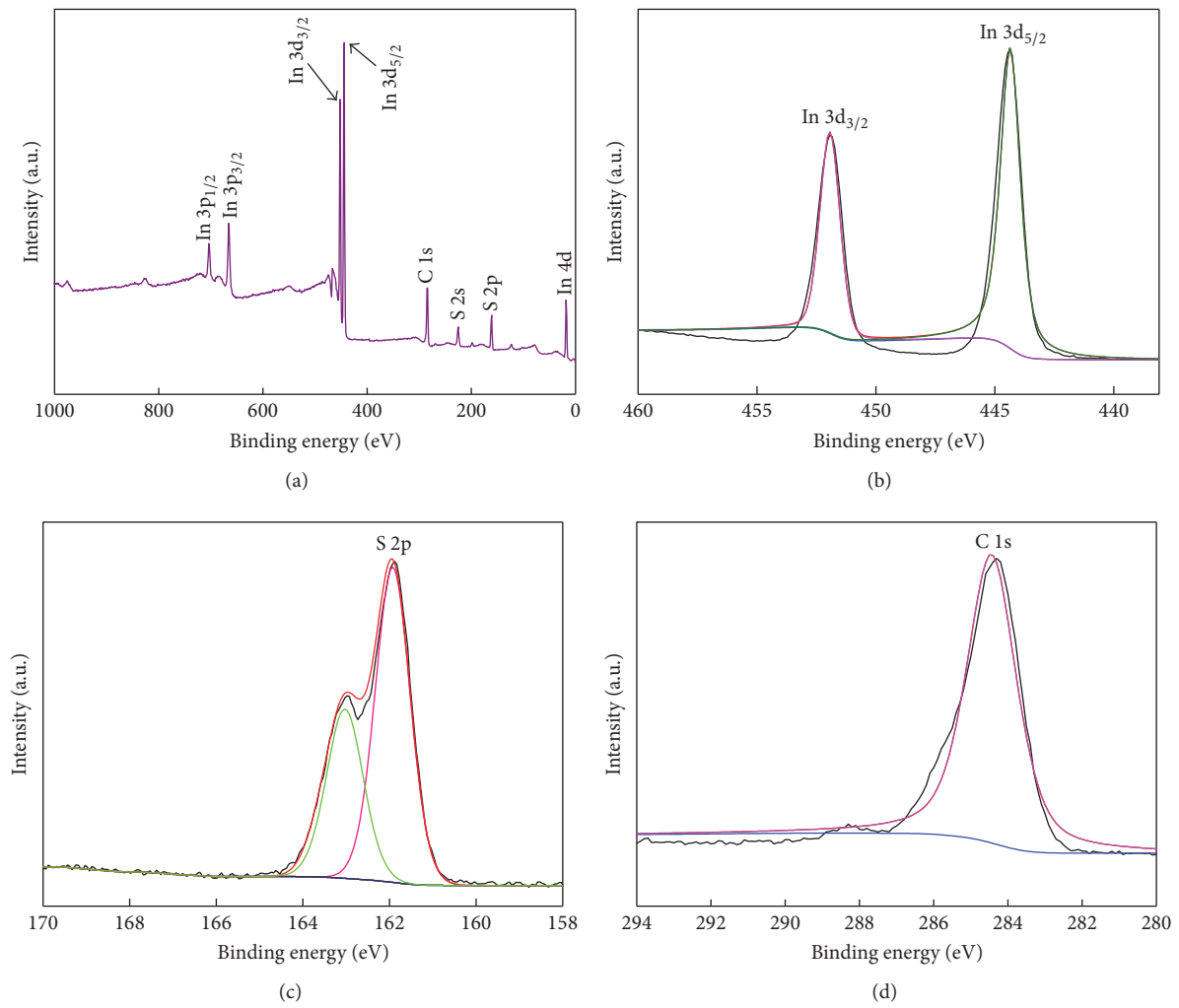
(a)

(b)

(c)

(d)

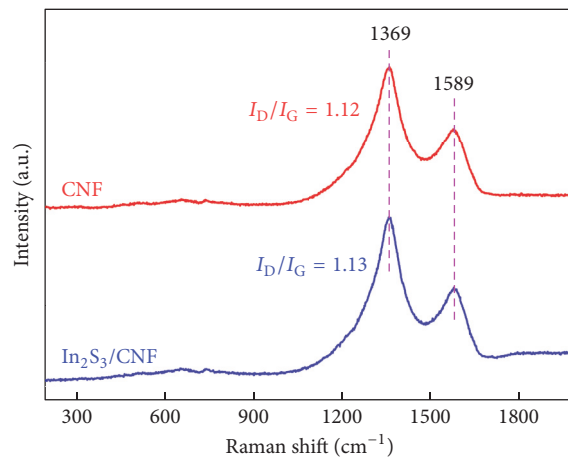FIGURE 4: XPS spectra of the $In_2S_3$/CNF-2: survey spectrum (a), In 3d (b), S 2p (c), and C 1s (d).



FIGURE 5: Raman spectra of CNF and $In_2S_3$/CNF-2.
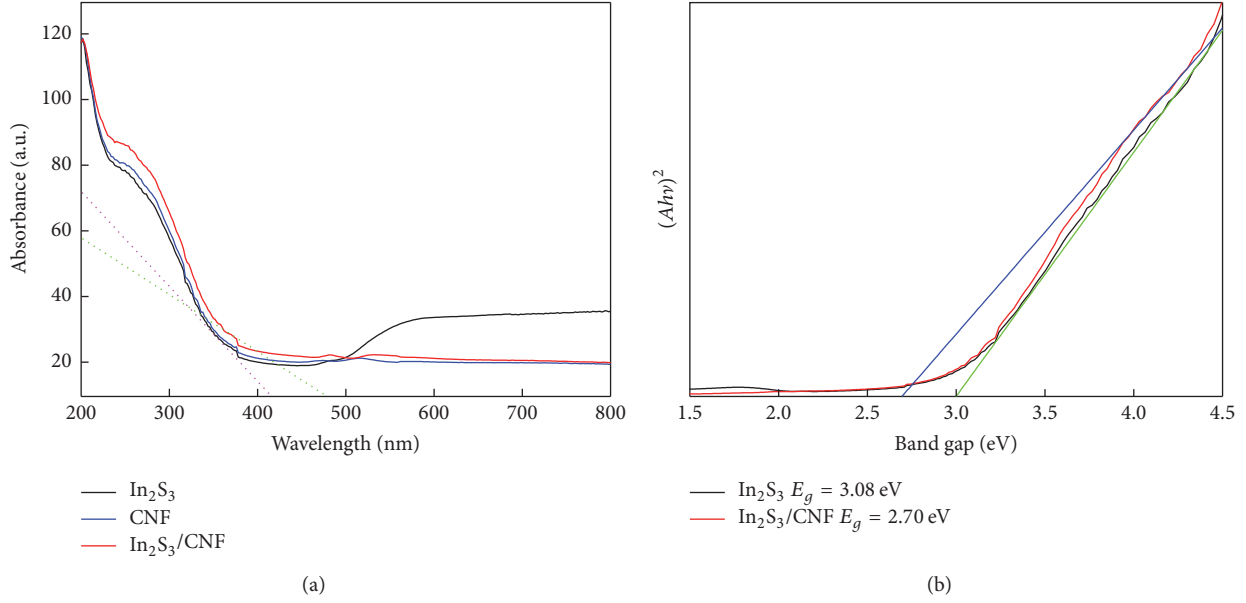
(a)



(b)

Figure 6: UV-vis diffuse reflectance spectrum of $In_2S_3$, CNF, and $In_2S_3$/CNF-2 (a) and the direct band gap determination of $In_2S_3$ and $In_2S_3$/CNF-2 (b). The tangent at this point corresponds to the smallest absorption wavelength.

and 7(b); the UV-vis absorption spectra in Figure 7 show the characteristic absorptions of RB at 570 and 580 nm. Owing to the strong absorption ability of CNF, a certain amount of RB was attached to the CNF before irradiation. Furthermore, when the dissociation and adsorption reach equilibrium, the concentration change of Rhodamine B, which is degraded by $In_2S_3$ and $In_2S_3$/CNF-2, is the same. The concentration of RB does not significantly change after irradiation as shown in Figure 7(a). The change in the concentration of RB in Figure 7(b) is significantly greater than Figure 7(a), which can be further confirmed through the change of solution color before and after degradation with different photocatalysts.
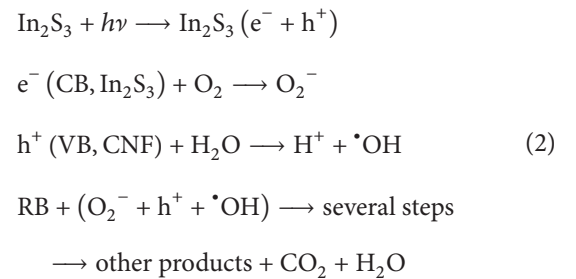
The degradation curves of RB on pure $In_2S_3$, CNF, and $In_2S_3$/CNF-2 composites were shown in Figure 8(a). Obviously, the concentration of CNF almost has no change, indicating that pure CNF has no photocatalytic activity under visible light irradiation. The $In_2S_3$/CNF-2 composites have a better photocatalyic efficiency (78.2%) for RB after visible light irradiation for 60 min than that of pure $In_2S_3$. It is concluded that $In_2S_3$/CNF-2 composites exhibited much higher photocatalytic efficiency compared with the pure $In_2S_3$. For a better comparison of the photocatalytic efficiency of $In_2S_3$/CNF-2 and pure $In_2S_3$, the kinetic analysis of degradation of RB was explored to confirm it. The above degradation reactions followed a Langmuir-Hinshelwood apparent first-order kinetics model [32, 35] when the initial concentrations of the reactants are less than 100 ppm. The Langmuir-Hinshelwood apparent first-order kinetics model is described below:

$$-\ln\left(\frac{C_0}{C}\right) = K_{app}t, \quad (1)$$

where $K_{app}$ is the apparent first-order rate constant ($min^{-1}$). The determined $K_{app}$ values for degradation of RB with different catalysts are presented in Figure 8(b). It is clear that the as-prepared $In_2S_3$/CNF-2 composites show the highest reaction rate among the two catalysts with $K_{app}$ = 0.0232 $min^{-1}$, while $K_{app}$ = 0.0169 $min^{-1}$ for pure $In_2S_3$. The photocatalytic reactivity order is well consistent with the activity studies above.

It is reasonable to presume that the photogenerated electrons ($e^-$) transfer from $In_2S_3$ to CNF in the $In_2S_3$/CNF system under visible light irradiation. Therefore, the photogenerated electrons first transfer to CNF and then are trapped by $O_2$ and $H_2O$ at the surface of photocatalyst or solution to form the active species such as $O_2^-$. These active species could help the degradation of RB dye. At the same time, the photogenerated holes ($h^+$) could react with $H_2O$ to form $^\bullet OH$, hydrogen ions ($H^+$), and then oxidize RB dye directly [12]. The complete photodegradation process can be summarized by the following reaction steps:

$$In_2S_3 + h\nu \longrightarrow In_2S_3\left(e^- + h^+\right)$$

$$e^-\left(CB, In_2S_3\right) + O_2 \longrightarrow O_2^-$$

$$h^+\left(VB, CNF\right) + H_2O \longrightarrow H^+ + {}^\bullet OH \quad (2)$$

$$RB + \left(O_2^- + h^+ + {}^\bullet OH\right) \longrightarrow \text{several steps}$$

$$\longrightarrow \text{other products} + CO_2 + H_2O$$

## 4. Conclusion

In summary, an effective method of preparing $In_2S_3$/CNF photocatalysts was described in this paper. The incorporation
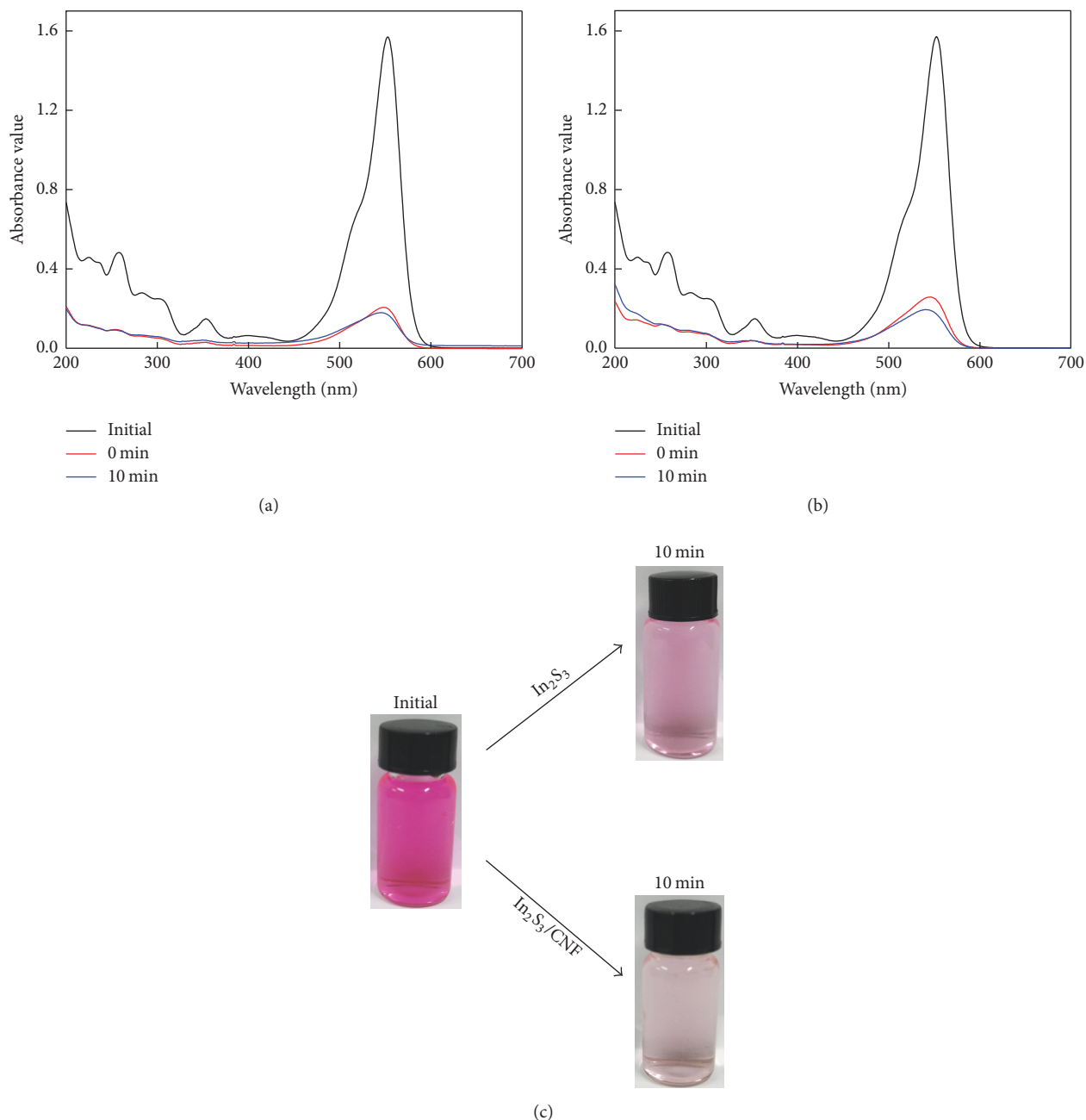
(a)



(b)



(c)

FIGURE 7: Removal efficiency of 50 mg/L RB solution during 10 min of irradiation with $In_2S_3$ (a) and $In_2S_3$/CNF-2 (b). The changes of solution color before and after degradation with different photocatalysts under visible light irradiation (c).

of CNF serving as electron collectors realizes a more effective separation of photogenerated electron-hole pairs and greatly boosts the photocatalytic activity of the products compared with the pure $In_2S_3$. The $In_2S_3$/CNF-2 composites show strong adsorption ability towards the RB, they can degrade 50 ppm of RB in 60 minutes under visible lights, and the excellent degradation RB activities of $In_2S_3$/CNF are mainly attributed to the large amount of effectively reactive species like $h^+$ and $O_2^-$. Overall, this study provides a new option to construct the semiconductor/CNF composites with high photocatalytic activity, environmental remediation, and energy conversion.

## Conflicts of Interest

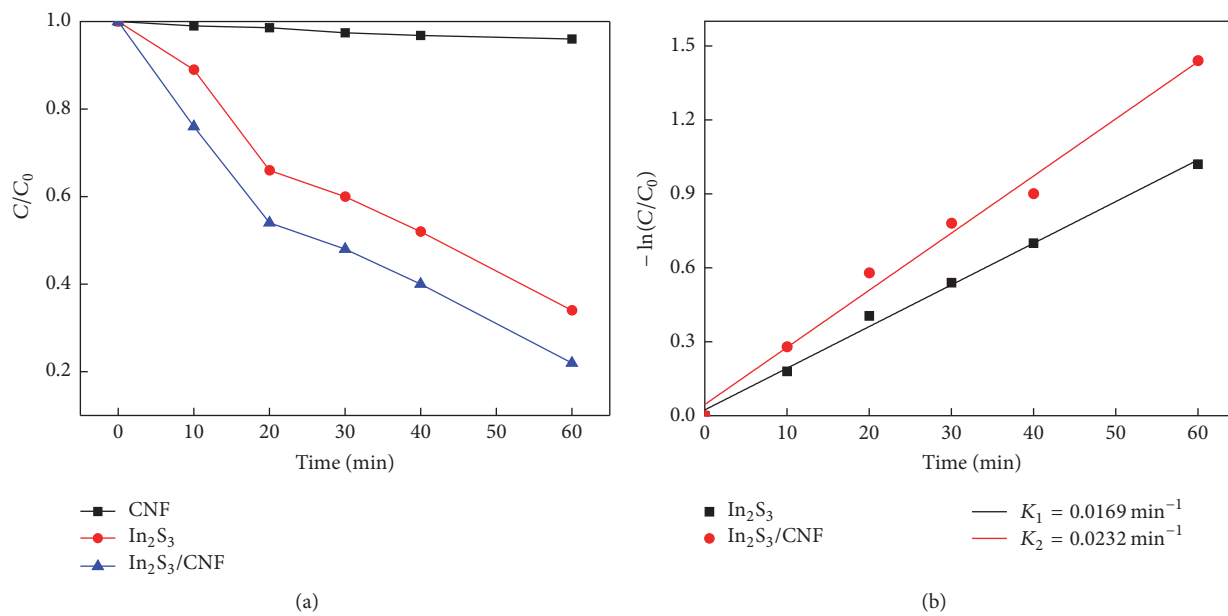The authors declare that they have no conflicts of interest.

(a)

(b)

FIGURE 8: Degradation curve of RB over different photocatalysts under visible light (a). Kinetic linear simulation curves of RB degradation over the different photocatalysts under visible light irradiation (b).
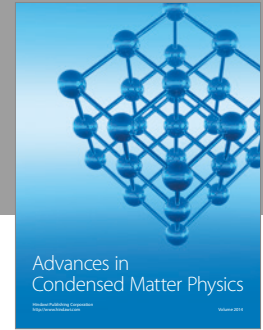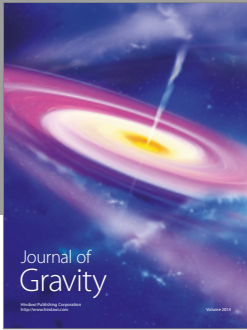
## References

[1] J. Gong and R. Luque, "Catalysis for production of renewable energy," *Chemical Society Reviews*, vol. 43, no. 22, pp. 7466–7468, 2014.

[2] S. J. A. Moniz, S. A. Shevlin, D. J. Martin, Z.-X. Guo, and J. Tang, "Visible-light driven heterojunction photocatalysts for water splitting-a critical review," *Energy & Environmental Science*, vol. 8, no. 3, pp. 731–759, 2015.

[3] T. Phongamwong, W. Donphai, P. Prasitchoke et al., "Novel visible-light-sensitized Chl-Mg/P25 catalysts for photocatalytic degradation of rhodamine B," *Applied Catalysis B: Environmental*, vol. 207, pp. 326–334, 2017.

[4] K. Kaygusuz, "Energy and environmental issues relating to greenhouse gas emissions for sustainable development in Turkey," *Renewable & Sustainable Energy Reviews*, vol. 13, no. 1, pp. 253–270, 2009.

[5] Z. Yang, L. Huang, Y. Xie et al., "Controllable synthesis of $Bi_2WO_6$ nanoplate self-assembled hierarchical erythro-cyte microspheres via a one-pot hydrothermal reaction with enhanced visible light photocatalytic activity," *Applied Surface Science*, vol. 403, pp. 326–334, 2017.

[6] Z. Ai, G. Zhao, Y. Zhong et al., "Phase junction CdS: High efficient and stable photocatalyst for hydrogen generation," *Applied Catalysis B: Environmental*, vol. 221, pp. 179–186, 2018.

[7] L. He, Z. Tong, Z. Wang, M. Chen, N. Huang, and W. Zhang, "Effects of calcination temperature and heating rate on the photocatalytic properties of ZnO prepared by pyrolysis," *Journal of Colloid and Interface Science*, vol. 509, pp. 448–456, 2018.

[8] Y. Li, G. Chen, Q. Wang, X. Wang, A. Zhou, and Z. Shen, "Hierarchical ZnS-In2 S3 -CuS nanospheres with nanoporous structure: Facile synthesis, growth mechanism, and excellent photocatalytic activity," *Advanced Functional Materials*, vol. 20, no. 19, pp. 3390–3398, 2010.

[9] W. Qiu, M. Xu, X. Yang et al., "Biomolecule-assisted hydrothermal synthesis of $In_2S_3$ porous films and enhanced photocatalytic properties," *Journal of Materials Chemistry*, vol. 21, no. 35, pp. 13327–13333, 2011.

[10] Y. Xing, H. Zhang, S. Song et al., "Hydrothermal synthesis and photoluminescent properties of stacked indium sulfide superstructures," *Chemical Communications*, no. 12, pp. 1476–1478, 2008.

[11] Y. Mi, H. Li, Y. Zhang, R. Zhang, and W. Hou, "One-pot synthesis of belt-like $Bi_2S_3$ /BiOCl hierarchical composites with enhanced visible light photocatalytic activity," *Applied Surface Science*, vol. 423, pp. 1062–1071, 2017.

[12] C. Yu, K. Wang, P. Yang et al., "One-pot facile synthesis of $Bi_2S_3$/$SnS_2$/$Bi_2O_3$ ternary heterojunction as advanced double Z-scheme photocatalytic system for efficient dye removal under sunlight irradiation," *Applied Surface Science*, vol. 420, pp. 233–242, 2017.

[13] Y. Yu, L. Yan, J. Cheng, and C. Jing, "Mechanistic insights into TiO 2 thickness in $Fe_3O_4$ @$TiO_2$-GO composites for enrofloxacin photodegradation," *Chemical Engineering Journal*, vol. 325, pp. 647–654, 2017.

[14] Y. Zhang, J. Chen, L. Hua et al., "High photocatalytic activity of hierarchical $SiO_2$ @C-doped $TiO_2$ hollow spheres in UV and visible light towards degradation of rhodamine B," *Journal of Hazardous Materials*, vol. 340, pp. 309–318, 2017.

[15] X. An, J. C. Yu, F. Wang, C. Li, and Y. Li, "One-pot synthesis of In2S3 nanosheets/graphene composites with enhanced visible-light photocatalytic activity," *Applied Catalysis B: Environmental*, vol. 129, pp. 80–88, 2013.

[16] J. Chen, W. Mei, Q. Huang et al., "Highly efficient three-dimensional flower-like AgI/Bi2O2CO3heterojunction with enhanced photocatalytic performance," *Journal of Alloys and Compounds*, vol. 688, pp. 225–234, 2016.

[17] Y. K. Kim, S. K. Lim, H. Park, M. R. Hoffmann, and S. Kim, "Trilayer CdS/carbon nanofiber (CNF) mat/Pt-TiO2 composite structures for solar hydrogen production: Effects of CNF mat thickness," *Applied Catalysis B: Environmental*, vol. 196, pp. 216–222, 2016.

[18] C. Luo, D. Li, W. Wu, C. Yu, W. Li, and C. Pan, "Preparation of 3D reticulated ZnO/CNF/NiO heteroarchitecture for high-performance photocatalysis," *Applied Catalysis B: Environmental*, vol. 166-167, pp. 217–223, 2015.

[19] M. Ouzzine, M. A. Lillo-Ródenas, and A. Linares-Solano, "Carbon nanofibres as substrates for the preparation of TiO 2 nanostructured photocatalysts," *Applied Catalysis B: Environmental*, vol. 127, pp. 291–299, 2012.

[20] W. Li, L. Zeng, Z. Yang et al., "Free-standing and binder-free sodium-ion electrodes with ultralong cycle life and high rate performance based on porous carbon nanofibers," *Nanoscale*, vol. 6, no. 2, pp. 693–698, 2014.

[21] L. Peng, L. Hu, and X. Fang, "Energy harvesting for nanostructured self-powered photodetectors," *Advanced Functional Materials*, vol. 24, no. 18, pp. 2591–2610, 2014.

[22] J. S. Im, M. I. Kim, and Y.-S. Lee, "Preparation of PAN-based electrospun nanofiber webs containing TiO2 for photocatalytic degradation," *Materials Letters*, vol. 62, no. 21-22, pp. 3652–3655, 2008.

[23] J. Chen, H. Wang, G. Huang et al., "Facile synthesis of urchin-like hierarchical $Nb_2O_5$ nanospheres with enhanced visible light photocatalytic activity," *Journal of Alloys and Compounds*, vol. 728, pp. 19–28, 2017.

[24] L. Zhang, W. Zheng, H. Jiu, W. Zhu, and G. Qi, "Preparation of the anatase/TiO2(B) TiO2 by self-assembly process and the high photodegradable performance on RhB," *Ceramics International*, vol. 42, no. 11, pp. 12726–12734, 2016.

[25] C. Mendoza, A. Valle, M. Castellote, A. Bahamonde, and M. Faraldos, "$TiO_2$ and $TiO_2$–$SiO_2$ coated cement: Comparison of mechanic and photocatalytic properties," *Applied Catalysis B: Environmental*, vol. 178, pp. 155–164, 2015.

[26] Y. Zhong, X. Qiu, D. Chen et al., "Flexible Electrospun Carbon Nanofiber/Tin(IV) Sulfide Core/Sheath Membranes for Photocatalytically Treating Chromium(VI)-Containing Wastewater," *ACS Applied Materials & Interfaces*, vol. 8, no. 42, pp. 28671–28677, 2016.

[27] J. Li, Y. Ma, Z. Ye et al., "Fast electron transfer and enhanced visible light photocatalytic activity using multi-dimensional components of carbon quantum dots@3D daisy-like In2S3/single-wall carbon nanotubes," *Applied Catalysis B: Environmental*, vol. 204, pp. 224–238, 2017.

[28] S. Stankovich, D. A. Dikin, R. D. Piner et al., "Synthesis of graphene-based nanosheets via chemical reduction of exfoliated graphite oxide," *Carbon*, vol. 45, no. 7, pp. 1558–1565, 2007.

[29] F. Tuinstra and J. L. Koenig, "Raman spectrum of graphite," *The Journal of Chemical Physics*, vol. 53, no. 3, pp. 1126–1130, 1970.

[30] S. Verma and R. K. Dutta, "Enhanced ROS generation by ZnO-ammonia modified graphene oxide nanocomposites for photocatalytic degradation of trypan blue dye and 4-nitrophenol," *Journal of Environmental Chemical Engineering (JECE)*, vol. 5, no. 5, pp. 4776–4787, 2017.

[31] S. Kment, Z. Hubicka, H. Kmentova et al., "Photoelectrochemical properties of hierarchical nanocomposite structure: Carbon nanofibers/TiO2/ZnO thin films," *Catalysis Today*, vol. 161, no. 1, pp. 8–14, 2011.

[32] S. Guo, Y. Zhu, Y. Yan, Y. Min, J. Fan, and Q. Xu, "Holey structured graphitic carbon nitride thin sheets with edge oxygen doping via photo-Fenton reaction with enhanced photocatalytic activity," *Applied Catalysis B: Environmental*, vol. 185, pp. 315–321, 2016.

[33] M. Tahir and N. Saidina Amin, "Photocatalytic reduction of carbon dioxide with water vapors over montmorillonite modified $TiO_2$ nanocomposites," *Applied Catalysis B: Environmental*, vol. 142-143, pp. 512–522, 2013.

[34] P. Zhang, C. Shao, Z. Zhang et al., "In situ assembly of well-dispersed Ag nanoparticles (AgNPs) on electrospun carbon nanofibers (CNFs) for catalytic reduction of 4-nitrophenol," *Nanoscale*, vol. 3, no. 8, pp. 3357–3363, 2011.

[35] L. Han, D. Mao, Y. Huang et al., "Fabrication of unique Tin(IV) Sulfide/Graphene Oxide for photocatalytically treating chromium(VI)-containing wastewater," *Journal of Cleaner Production*, vol. 168, pp. 519–525, 2017.